International Journal of Hydrogen Energy 63 (2024) 896–904

Contents lists available at ScienceDirect

International Journal of Hydrogen Energy

journal homepage: www.elsevier.com/locate/he

Engineering the heterojunction between TiO_2 and In_2O_3 for improving the solar-driven hydrogen production

Salvatore Impemba [a,b], Giacomo Provinciali [a], Jonathan Filippi [a], Cristina Salvatici [a], Enrico Berretti [a,c], Stefano Caporali [d], Martina Banchelli [e], Maria Caporali [a,*]

[a] CNR-ICCOM, Via Madonna Del Piano 10, 50019, Sesto Fiorentino, Italy
[b] CSGI, Department of Chemistry, University of Florence, Via Della Lastruccia 3, 50019, Sesto Fiorentino, Italy
[c] INSTM, Via G. Giusti 9, 50121, Firenze, Italy
[d] Department of Industrial Engineering, University of Florence, Via di S. Marta 3, 50139, Firenze, Italy
[e] CNR-IFAC, Via Madonna Del Piano 10, 50019, Sesto Fiorentino, Italy

ARTICLE INFO

Handling editor: Jinlong Gong

Keywords:
Cuprous oxide
Hydrogen
Indium oxide
Photocatalysis
Titania
Thermal annealing

ABSTRACT

Nanostructured In_2O_3 was grown on TiO_2 NPs by thermal treatment of the solids mixture of TiO_2 with the parent $In(OH)_3$. The effect of calcination temperature in the range between 400 °C and 700 °C was investigated and peculiar changes both in the structure and in the catalytic activity of the TiO_2/In_2O_3 heterostructure were revealed. It was found out that T = 600 °C is the best operating temperature for hydrogen production and in combination with 3.5 wt% In_2O_3 the H_2 production from water reached the value of 3.5 mmol/h·g irradiating in the UV–Vis region. Once 5.0 wt% Cu_2O nanoparticles were loaded on TiO_2/In_2O_3, the photocatalytic activity boosted to 9.6 mmol/h·g of H_2, overcoming the hydrogen production of pristine TiO_2 by a factor of 48. This result can be attributed to the formation of a highly efficient heterojunction that assures a synergistic cooperation among the three semiconductors yielding an improved charge separation and faster charge transport, as evidenced by Mott-Schottky, PL and EIS measures.

1. Introduction

Hydrogen represents one of the most promising energy resources to replace fossil fuels due to its high energy density and zero emission pollution [1,2]. Among the various means for producing hydrogen, the water splitting reaction through solar-driven technology is one of the most studied process since it is eco-friendly, requires a low energy input and there is no secondary pollution discharge [3,4]. One of the aims of scientific research is the development of ever more efficient photocatalysts in this field [5–8]. Titanium dioxide has a widespread use in photocatalysis and surely it is the most common semiconductor for this application due to its high chemical stability, low price, and nontoxicity. Nevertheless, the use of bare TiO_2 as a photocatalyst is affected by some drawbacks as low sunlight use efficiency and fast recombination of photo-generated carriers [9–11]. In particular in the photocatalytic H_2 production, bare TiO_2 has quite low quantum efficiency, thus a common strategy to face the drawbacks has been the pairing of TiO_2 with suitable semiconductors and the use of sacrificial agents to improve light harvesting efficiency and photocatalytic performance [12,13]. Several studies have shown that indium represents a highly promising photocatalyst [14–18], since it decreases charge carrier recombination moreover it is non-toxic and largely available (compared to pricy noble metals as Pd, Pt and Au). In_2O_3, being a semiconductor with an indirect band gap of 2.8 eV and a direct band gap of ca. 3.2 eV, is known as an efficient sensitizer able to expand the absorption from UV to visible region [19]. TiO_2 has a band gap of ~3.2 eV in which both the conduction and valence band (E_{CB} = −0.4 V, E_{VB} = 2.8 eV vs NHE) lie underneath those of In_2O_3 (E_{CB} = −0.63 V vs NHE, E_{VB} = 2.17 eV), thus yielding a type II heterojunction which is known to be ideal for the photocatalytic efficiency [20]. A variety of In_2O_3/TiO_2 nanocomposites have been studied showing improved photocatalytic activity in the reduction of CO_2 to CH_4 [21], in the degradation of methyl orange [22] and in H_2 evolution [23–25].

In the present work, starting from commercial TiO_2 P25 (anatase 80%, rutile 20%) nanoparticles, the formation of a TiO_2-based heterostructure was envisaged by the coupling with In_2O_3 and Cu_2O in the quality of narrower band gap semiconductors, with the aim to enhance the absorbance towards the visible region and increase the solar light-to-

* Corresponding author.
E-mail address: maria.caporali@iccom.cnr.it (M. Caporali).

https://doi.org/10.1016/j.ijhydene.2024.03.162
Received 18 December 2023; Received in revised form 4 March 2024; Accepted 11 March 2024
Available online 23 March 2024

energy conversion.

The hybridization of TiO_2 with In_2O_3 nanorods was performed in two different ways: a) by mixing preformed In_2O_3 with TiO_2 via ultrasonication in solution, b) by direct growth of In_2O_3 nanostructures on TiO_2, via calcination of $In(OH)_3$ mixed with TiO_2 NPs. Additionally, the calcination temperature was varied from 400° to 700 °C and the effects of thermal treatment on the X-ray structure and catalytic activity of the binary TiO_2/In_2O_3 were evaluated. To further improve the photocatalytic activity, Cu_2O nanoparticles were loaded on the binary TiO_2/In_2O_3. Indeed, cuprous oxide is a well-known p-type semiconductor [26], with a narrow band gap (2.0–2.6 eV) and is usually paired with TiO_2 due to its considerable absorbance in the visible region [27]. Additionally, being TiO_2 and In_2O_3 n-type semiconductors, the creation of a p-n heterojunction would certainly strengthen the efficiency of charge transport. Satisfyingly, the new ternary photocatalyst gave an excellent hydrogen production of 9.6 mmol/h·g, which is 48 times higher than pristine TiO_2. As added value, the new photocatalyst does not contain any noble metal and can be prepared by an easily scalable and straightforward synthesis.

2. Experimental section

2.1. Materials and chemicals

TiO_2 P25 was obtained from Degussa, Indium (III) chloride hydrate ($InCl_3{\cdot}4H_2O$, 99.99%), urea (99%), hydrazine $N_2H_4{\bullet}H_2O$ (98% in water) were purchased from Merck. All reagents were used without further purification.

2.2. Synthesis of In_2O_3

$InCl_3$ $4H_2O$ (146.6 mg, 0.5 mmol) and urea (120.1 mg, 2.0 mmol) were dissolved by stirring for 30 min in 40 mL of distilled and degassed water, for a final concentration of 0.012 M. The solution was transferred into a Teflon-lined autoclave (volume of 50 mL) and heated at 140 °C in an oven, for 16 h. Then, the autoclave was cooled at room temperature and the white solid product was isolated by centrifugation. Six washing/centrifugation cycles (8000 rpm for 20 min) were carried out, four using distilled water and two using ethanol. The white solid of $In(OH)_3$ was collected and dried under vacuum for 6 h. Its chemical identity and purity was assessed by XRD, see Fig. S2. Afterwards, it was annealed at 600 °C for 2 h in argon flow with a heating rate of 10 °C/min, obtaining a pale yellow powder. Yield (respect to starting $InCl_3$): 58%.

2.3. Synthesis of TiO_2/In_2O_3 heterostructure via sonication, TiO_2/In_2O_{3sonic}

In_2O_3 (1.5 mg) previously synthetized and TiO_2 P25 (41.4 mg) were ultrasonicated for 2 h in 28 mL of isopropanol. To the suspension of TiO_2/In_2O_3, ethanol (10 mL) was added and after centrifugation the solid was isolated and dried under vacuum overnight.

2.4. Synthesis of TiO_2/In_2O_3 heterostructure via thermal treatment, TiO_2/In_2O_{3calc}

The x % In_2O_3/TiO_2 (0.5, 1.5, 3.5, 5 wt%) catalysts with different contents x% of In_2O_3, were prepared by a thermal process. The calculated amounts of $In(OH)_3$ powder (5.3 mg in the case of 3.5 wt%) were mixed with TiO_2 (121.6 mg) in 50 mL degassed water and ultrasonicated for 1 h. One washing/centrifugation cycle was carried out adding degassed acetone (10 mL), then the isolated solid was dried under vacuum overnight and annealed in a muffle furnace at 600 °C for 2 h in argon flow, with a heating rate of 10 °C/min. Yield: 98%. The samples with different contents of In_2O_3 were obtained and denoted as x% In_2O_3/TiO_2.

2.5. Synthesis of TiO_2/In_2O_3 heterostructure at different calcination temperature

Since the best performing catalyst resulted TiO_2/In_2O_3 3.5 wt%, the corresponding parent composite $TiO_2/In(OH)_3$ was annealed in a quartz tubular furnace in argon atmosphere for 2 h at 400°, 500° and 700 °C respectively with a heating rate of 10 °C/min to study the role of annealing temperature in the catalytic activity. The exact In/Ti ratio was assessed by ICP analysis as shown in Table S1.

2.6. Synthesis of Cu_2O nanoparticles

$CuCl_2$ (23.5 mg, 0.17 mmol) was solubilized in 16 mL of degassed H_2O (Solution A) and ultrasonicated for 10 min. Afterwards, $N_2H_4{\bullet}H_2O$ (hydrazine, 26.0 mg, 0.52 mmol, 3 equiv) was solubilized in 16 mL of degassed H_2O (Solution B). Then, Solution B was added into Solution An under stirring and quickly an orange suspension was obtained. The latter was stirred at 900 rpm for 2 h at room temperature under nitrogen atmosphere, then the orange powder of Cu_2O was isolated by centrifugation. Three washing/centrifugation cycles were carried out, two using degassed H_2O and one using degassed acetone, then the solid was dried under vacuum overnight.

2.7. Synthesis of the ternary heterostructure $TiO_2/In_2O_3/Cu_2O$

Three ternary composites were prepared by adding a variable amount of Cu_2O NPs (2.5, 5.0, 7.5 wt%) to the binary TiO_2/In_2O_3 having 3.5 wt% In_2O_3.

In_2O_3/TiO_2 (19 mg) previously synthetized, see section 2.4, and Cu_2O (1 mg) were ultrasonicated for 3 h in 13 mL of degassed isopropanol. To the suspension, degassed ethanol was added and after centrifugation the light orange solid was isolated and dried under vacuum overnight.

2.8. Characterization of samples

To investigate the surface morphology, secondary electron images were acquired by a Scanning Electron Microscopy (SEM) (Gaia 3 by Tescan), using an accelerating voltage of the electron beam of 5 kV. To assess the elemental distribution in the sample, STEM EDX mapping was also performed using a 200 kV HR-TEM (Talos F200X G2 by Thermo Fisher Scientific).

To determine the crystallinity and purity of the synthesized catalyst, X-ray diffraction (XRD) (Panalytical Advance X-ray powder diffractometer) was performed.

X-ray Photoelectron Spectroscopy (XPS) measurements were performed at the Chemistry Department, University of Florence (Italy) in an ultra-high vacuum (10^{-9} mbar) system equipped with a VSW HAC 5000 hemispherical electron energy analyzer and a non-monochromatized Mg-Kα X-ray source (1253.6 eV). The source power used was 100 W (10 kV × 10 mA) and the spectra were acquired in the constant-pass-energy mode at E_{pas} = 44 eV. The overall energy resolution was 1.2 eV as a full-width at half maximum (FWHM) for the Ag $3d_{5/2}$ line of a pure silver reference. The recorded spectra were calibrated using C 1s peak of adventitious carbon as an internal standard (284.8 eV) and, after subtraction of a Shirley-type background, fitted using XPS Peak 4.1 software employing Gauss-Lorentz curves. The samples were dropcasted from a suspension in methanol, dried under a stream of nitrogen and introduced in the UHV system via a loadlock under inert gas (N_2) flux, in order to minimize the exposure to air contaminants and kept in the introduction chamber for at least 12 h before the measurements.

The diffuse reflectance spectra were measured by a Shimadzu UV-2600 spectrometer on the solid samples using an integrating sphere with $BaSO_4$ as a reference material. By using the Kubelka-Munk equation, Tauc plots were obtained and the optical band-gap energy of the samples was extrapolated.

Raman characterization of the samples was performed at room temperature in a backscattering configuration using a LabRam HR 800EVO Raman spectrometer (Horiba France SAS) equipped with an Olympus BXFM microscope (objective ×100, NA 0.9), TE cooled CCD detector (Syncerity OE), 532 nm laser and 600 grooves/mm diffraction grating. The spectral resolution was 0.9–1.8 cm^{-1}. The sample was drop-casted on silicon wafer as the substrate then it was dried in nitrogen atmosphere. The laser power at the sample was 3.6 mW and the acquisition time was 5 s. Ten to twenty spectra were registered for each sample at different locations to verify sample homogeneity and the absence of photoinduced phenomena. The reference spectrum of Si was measured contextually in each sample. Raman spectra were corrected for the baseline and Raman peak analysis was performed through a mixed Gaussian-Lorentzian fitting function to calculate position and area of the characteristic peaks.

Photoluminescence spectroscopy (PL) were registered using a Jasco spectrofluorometer model FP-8300. The powder samples were analysed by irradiating at a wavelength close to the maximum absorption in the corresponding UV–Vis spectrum, i.e. $\lambda = 325$ nm.

Electrochemical measurements including electrochemical impedance spectroscopy (EIS) and electrochemical response (cyclic voltammetry, CV) were carried out in a standard three electrode cell using an electrochemical workstation (PARSTAT 2273 potentiostat/galvanostat). The EIS (perturbation voltage 20 mV, frequency 100 KHz – 100 mHz) and CV were measured using a saturated Ag|AgCl|KCl reference electrode, a platinum coiled wire as the counter electrode and 0.5 M Na_2SO_4 aqueous solution as electrolyte. To prepare the working electrode, the standard TiO_2 P25 and the synthesized samples In_2O_3, Cu_2O, TiO_2/In_2O_{3calc}, TiO_2/In_2O_{3sonic} and $TiO_2/In_2O_3/Cu_2O$ nanocomposites were first dispersed in MeOH (1.0 mL). The dispersion containing the catalyst (3.0 mg/mL) was deposited by drop-coating on a fluorine-doped tin oxide (FTO) conductive glass substrate (2.0 cm^2) and was dried under a stream of nitrogen before measurements. Mott-Schottky (M − S) curves were measured under an AC amplitude of 10 mV and frequency of 1 kHz.

2.9. Photocatalytic performance tests

The evolution of hydrogen from water was carried out in a 12 mL cylindrical quartz tube closed with a rubber cap having a silicone septum under the irradiation of a 300 W Xe lamp (Newport, USA), see Fig. S1 for the image of the photocatalytic equipment. The photocatalyst (1.3 mg) was dispersed in 2.4 mL of degassed MilliQ water and 0.6 mL of degassed methanol (20 vol%) by 10 min ultrasonication. Then, the irradiation was started in the range UV–Vis (330–780 nm) and the system was kept to react under stirring at room temperature (T = 25 °C) for the required time. Every hour, the gases were sampled via a syringe and injected into a Shimadzu GC-2010 gas chromatograph equipped with an MS-5A column and a thermal conductivity detector using a temperature ramp program starting from 140 °C for 9 min and rising to 225 °C in 25 min, hydrogen retention time is 3.35 min.

3. Results and discussion

3.1. Synthesis and characterization of the photocatalysts

TiO_2 (P25) nanoparticles and nanostructured $In(OH)_3$ were mixed together by sonication and calcined at different temperature in the range 400–700 °C, yielding a series of samples TiO_2/In_2O_3calc. As a comparison, preformed In_2O_3 was sonicated with TiO_2 obtaining by self-assembly the sample TiO_2/In_2O_3sonic. As further step, Cu_2O NPs were integrated to the best performing binary, i.e. TiO_2/In_2O_3calc, giving the ternary photocatalyst $TiO_2/In_2O_3/Cu_2O$.

Fig. 1 shows XRD spectra of pristine TiO_2, In_2O_3 and Cu_2O, TiO_2/In_2O_3 obtained by calcination and the ternary nanocomposite $TiO_2/In_2O_3/Cu_2O$.

The diffraction peaks of anatase [28] TiO_2 appeared at $2\theta = 25.3°$ (011), 37.7° (004), 48.0° (020), 62.7° (024) and 75.0° (125) as shown in Fig. 1, bottom track. The diffraction peaks of rutile are much less intense (being around 20 wt%, for clarity are not indexed in the track in Fig. 1) and were observed at $2\theta = 27.4°$ (110), 36.1° (011), 41.2° (111), 54.3° (121), 69.0° (031), and 69.8° (112) in agreement with literature [29].

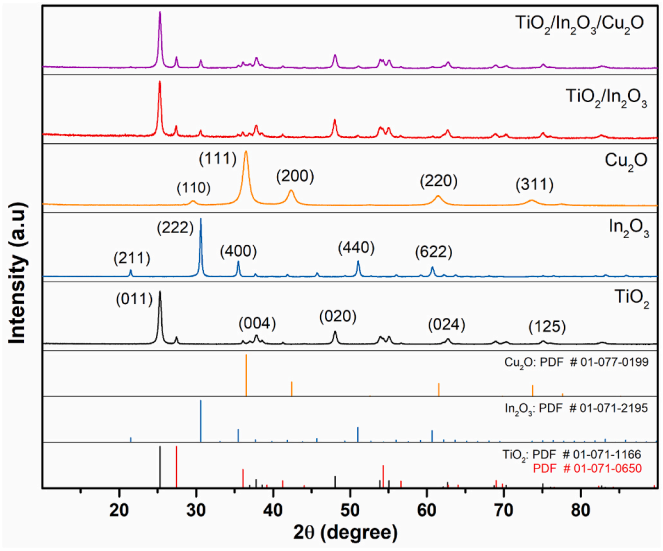

Fig. 1. Pxrd of TiO_2, In_2O_3, Cu_2O, TiO_2/In_2O_3 and $TiO_2/In_2O_3/Cu_2O$.

The reflections observed for In_2O_3 at $2\theta = 30.5°$, 35.4°, 45.6°, 51.0°, 60.6°, see Fig. 1 blue track, correspond to a cubic phase whose structural symmetry is governed by the *Ia*3 space group (ICDD #98-000-6517) [30]. The precursor $In(OH)_3$ has peaks at 22.3°, 31.7°, 39.1°, 45.4°, 51.2° and 56.9° as shown in Fig. S2, which agrees well with the cubic phase, possessing a space group symmetry of Im3 (ICDD #98-001-7283) [31]. The XRD pattern of Cu_2O shows diffraction peaks at 29.5°, 36.4°, 42.3°, 61.3°, and 73.5°, where the strong peak at 36.4° indexed to (111) plane shows that the preferred crystal orientation of Cu_2O NPs is cubic [32]. There are no diffraction peaks attributable to impurities of CuO and/or Cu, therefore the experimental procedure affords highly crystalline and pure Cu_2O NPs.

The diffraction peaks of binary TiO_2/In_2O_3 and ternary $TiO_2/In_2O_3/Cu_2O$ correspond to the standard card of TiO_2, In_2O_3 and Cu_2O thus confirming the composites were successfully fabricated.

Varying the calcination temperature of $TiO_2/In(OH)_3$ 3.5 wt% in the range 400°–700 °C, in the final compound there are only changes for the structure of TiO_2 where there is a net increase in rutile content respect to anatase when heating at 700 °C for 2 h, see Fig. S3.

Fig. 2 shows Raman spectra of pristine TiO_2, In_2O_3, TiO_2/In_2O_3 3.5 wt% calcined, TiO_2/In_2O_3 3.5 wt% sonicated and the ternary $TiO_2/In_2O_3/Cu_2O$. The vibrational signals for pristine TiO_2 NPs appeared at ν = 143 cm^{-1}, 195 cm^{-1}, 392 cm^{-1}, 513 cm^{-1} and 634 cm^{-1} which correspond respectively to $E_{g(1)}$, $E_{g(2)}$, B_{1g}, $A_{1g} + B_{1g(2)}$ and $E_{g(3)}$ characteristic vibrational modes of anatase [33]. Regarding In_2O_3 the Raman modes at 135, 307, 366, 495 and 631 cm^{-1} confirm the cubic structure [34] already observed by XRD, and well agree with literature [35]. For the binary TiO_2/In_2O_3 composite prepared by sonication, the Raman peaks of pristine TiO_2 and In_2O_3 are observed with no detectable changes with respect to the spectrum of single compounds. On the other hand, the Raman spectrum of TiO_2/In_2O_3 obtained by calcination reveals a red shift of the 307 cm^{-1} signal of In_2O_3, as shown in the inset of Fig. 2, and a broadening of the same peak with a change in full width at half maximum. These spectral changes are frequently observed due to the formation of new bonds between the oxygen of In_2O_3 and a dopant, as observed in doped-In_2O_3 nanocrystals [36]. In our system, the observed Raman changes of In_2O_3 can be ascribed to the interaction between In_2O_3 and Ti^{4+}, seemingly indium can diffuse in the crystal

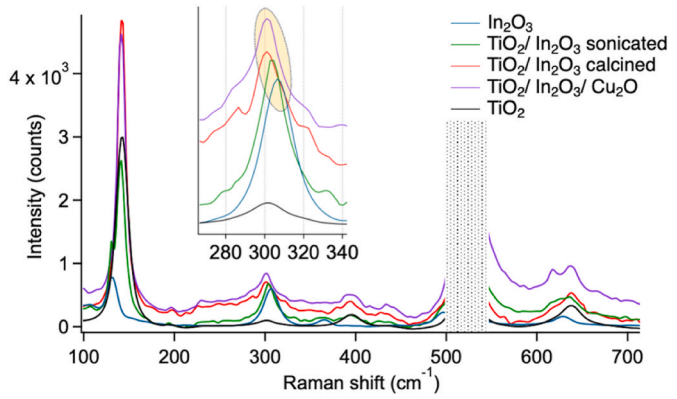

Fig. 2. Raman spectra of In_2O_3, TiO_2, TiO_2/In_2O_3 calcined, TiO_2/In_2O_3 sonicated and $TiO_2/In_2O_3/Cu_2O$ at 532 nm laser excitation. The peak of the silicon wafer at $\nu = 520$ cm^{-1} where it was deposited the sample, was subtracted for clarity from all the spectra. Inset shows the shifting behavior of In_2O_3 peak observed at 307 cm^{-1}. (For interpretation of the references to colour in this figure legend, the reader is referred to the Web version of this article.)

lattice of the TiO_2 matrix, with formation of TiO_2/In_2O_3 heterojunction which in turns favors an enhancement of the electron transfer and thus leads to an improved performance in catalysis, as it will be shown later on.

SEM images of $In(OH)_3$, In_2O_3, In_2O_3 grown on TiO_2 and the ternary composite $TiO_2/In_2O_3/Cu_2O$ are collected in Fig. 3 a,b,d and f respectively, together with a reference image of spherical TiO_2 NPs (see Fig. 3c) having average size 26 nm, see Fig. S4a for the relative size distribution. $In(OH)_3$ resulted constituted mainly by nanocubes with 0.5–1.5 μm of lateral length, in mixture with nanorods, having length between 0.8 and 3.0 μm and a diameter in the range 200–400 nm (Fig. 3a). After annealing $In(OH)_3$ at T = 600 °C for 2 h to produce In_2O_3, an intriguing change in structure can be seen (Fig. 3b). While the nanorods are almost unaffected by calcination, there is a dramatic effect on the nanocubes, which appear as teared apart and shattered with irregular edges and wrinkled surface. Once $In(OH)_3$ is calcined in mixture with TiO_2 NPs, the binary composite TiO_2/In_2O_3 is obtained and the morphology for In_2O_3 is the same as above described, with TiO_2 NPs distributed on its surface and edges (Fig. 3d and Fig. S5 for a panoramic view of TiO_2/In_2O_3). As third step, preformed Cu_2O NPs having average size of 220 nm (Fig. 3e and Fig. S4b for the size distribution) are added to the binary TiO_2/In_2O_3 by ultrasonication. Inspection by SEM on the as-synthesized ternary composite (Fig. 3f) shows a similar particle distribution respect to TiO_2/In_2O_3 (Fig. 3d) with a complete disappearance of Cu_2O NPs. Only a STEM EDX mapping (Fig. 4) confirms the presence of the Cu_2O NPs, which appear always buried beneath the fine TiO_2 dispersion. HRTEM on the ternary composite showed for TiO_2 NPs clear lattice fringes of anatase (101) (see Fig. S6) meaning the sonication or calcination step has not affected the size or morphology.

XPS measurements were carried out to obtain information on the chemical state of the elements in the binary and ternary nanocomposite. Fig. 5 shows the binding energy of Ti $2p_{3/2}$ and Ti $2p_{1/2}$ in pure TiO_2 which is located at 458.1 eV and 463.8 eV respectively, and this is consistent with Ti^{4+} in the TiO_2 lattice [37]. After forming the heterojunction with In_2O_3, these two peaks exhibited shifts to higher binding energies (BE) going to 458.7 eV and 464.4 eV respectively, that means an increase of 0.6 eV respect to pure TiO_2 with an unaltered spin-orbital splitting of 5.7 eV (as observed above) confirming the presence of Ti^{4+}. The increase in binding energy corresponds to a decrease of electron concentration in titanium, indicating the presence of a strong interaction likely due to Ti–O–In bond formation. Going to the ternary nanocomposite after assembly with Cu_2O NPs, the Ti 2p peaks shift at 458.3 eV and 464.1 eV respectively, thus exhibiting a lower shift (+0.3 eV) in BE respect to pristine TiO_2 [38]. Concerning XPS of In 3d, the spectrum is well resolved for TiO_2/In_2O_{3sonic} obtained by sonicating the two oxides, and shows the two characteristic peaks at B.E. = 443.8 eV and B.E. = 451.3 eV corresponding to In $3d_{5/2}$ and In $3d_{3/2}$ respectively, see Fig. S8. This is superimposable to the XPS In 3d spectrum observed for the synthetized In_2O_3, see Fig. S7 [39]. Surprisingly, in the TiO_2/In_2O_{3calc} and corresponding ternary $TiO_2/In_2O_{3calc}/Cu_2O$ composite, the

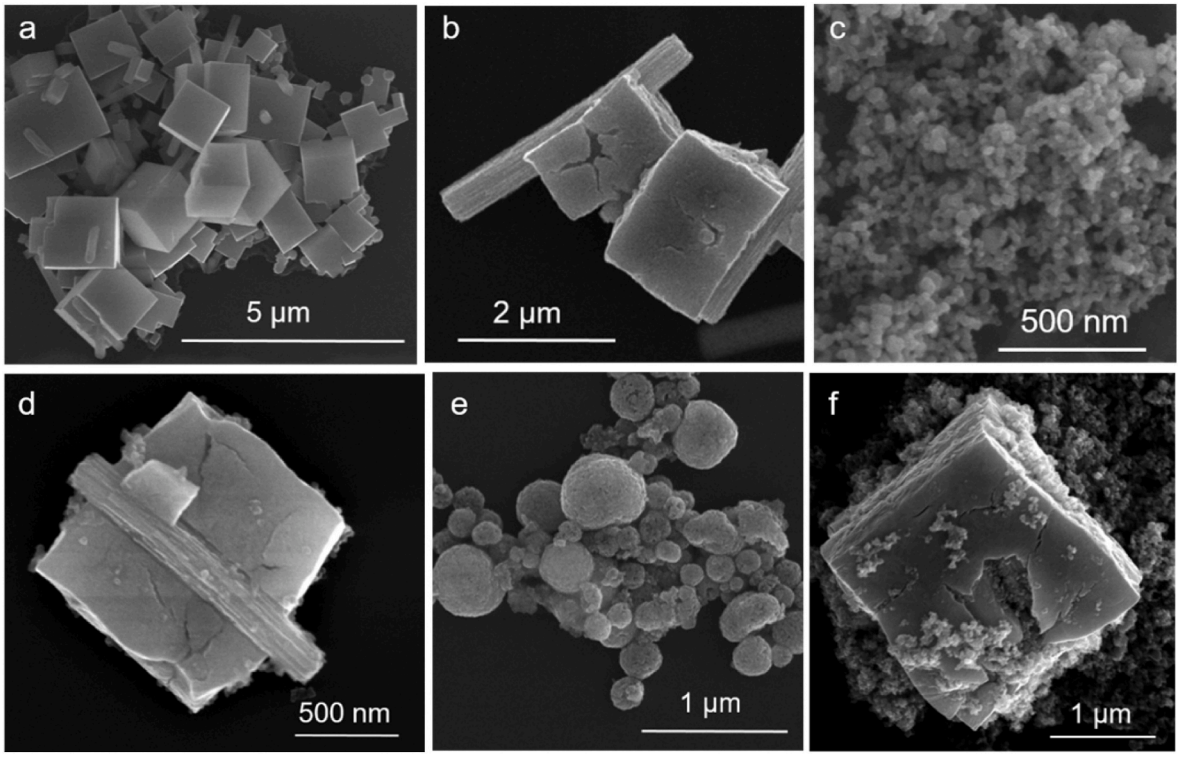

Fig. 3. SEM analysis of a) $In(OH)_3$; b) In_2O_3; c) TiO_2 NPs; d) In_2O_3 grown on TiO_2, e) Cu_2O NPs, f) $TiO_2/In_2O_3/Cu_2O$ composite.

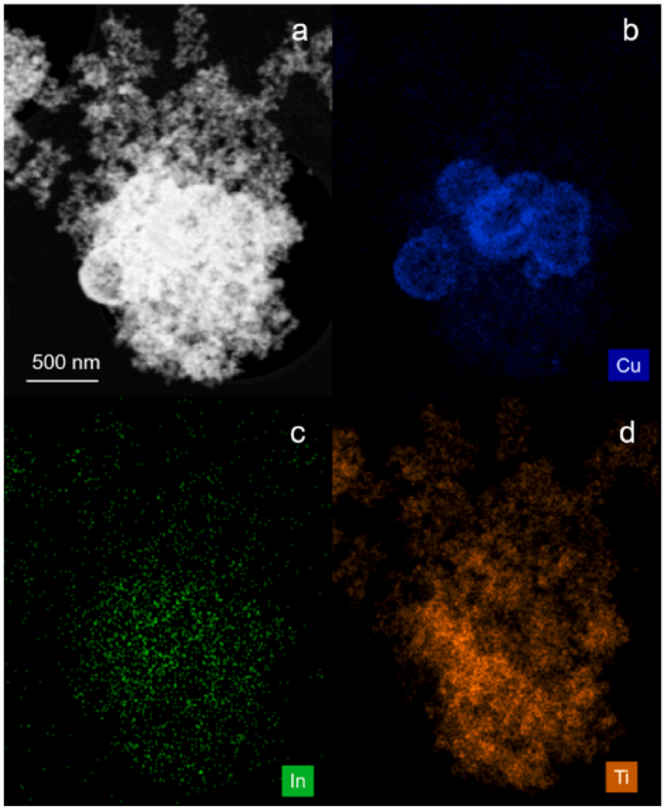

Fig. 4. HAADF-STEM image of $TiO_2/In_2O_3/Cu_2O$ (a) and relative EDX mapping images, b) Cu, c) In, d) Ti. Scale bar = 500 nm.

signal of In 3d is not distinguishable from the noise level. Being XPS a surface-sensitive technique, the absence of indium signal means there is a diffusion of this species from the surface into the bulk that reduces drastically its concentration at the surface. The XPS spectrum of core level Cu 2p shows Cu^+ as a largely predominant specie in the ternary nanohybrid, which is characterized by the Cu $2p_{3/2}$ component at B.E. = 932.7 eV and the Cu $2p_{1/2}$ component at B.E. = 952.2 eV; as a minor specie is present the oxide CuO as revealed by the peaks at B.E. = 934.9 eV, 954.7 eV and the shake-up peak in the region 938.6–947.5 eV which is diagnostic of the oxide [40].

In order to examine the light absorption properties, the samples were characterized by ultraviolet–visible diffuse reflectance spectroscopy (UV–Vis DRS). As displayed in Fig. 6, pure TiO_2 can only absorb light in the UV region and pure In_2O_3 absorbs light with wavelength less than 440 nm. As shown in Fig. 6a, the absorption of TiO_2/In_2O_3 and $TiO_2/In_2O_3/Cu_2O$ nanocomposites exhibits a red shift, indicating that the composites have stronger light absorption capabilities, which means the generation of more photo-generated electrons and holes. The optical band gap energy E_g was estimated by using *Kubelka-Munk* formula: $(\alpha h\nu)^n = k(h\nu - Eg)$ where α represents the absorption coefficient, k is a constant, $h\nu$ represents photon energy, n is equal to 2 and 1/2 for direct and indirect band gap semiconductors, respectively. TiO_2 is an indirect band gap semiconductor, meanwhile In_2O_3 and Cu_2O are direct semiconductor and from the Tauc plot resulted a band gap of 3.25 eV, 3.22 eV and 2.65 eV respectively [41,42]. The band gap energies of TiO_2/In_2O_3(3.5 wt%) and TiO_2/In_2O_3(3.5 wt%)/Cu_2O(5%) are 3.13 eV and 3.06 eV respectively, smaller than that of pure TiO_2. The decreased bandgap may be attributed to the formation of a heterojunction between the semiconductors with formation of a new photo-generated electron transport channel [43]. The results show that the ternary nanocomposite can much more effectively absorb and utilize visible light than pristine TiO_2.

To calculate the conduction band (CB) and valence band (VB) energy levels of TiO_2, In_2O_3, Cu_2O and their binary and ternary composite, electrochemical impedance measurements were carried out and the corresponding Mott-Schottky plots are shown in Fig. 7. From the extrapolation of the linear region of the Mott-Schottky plot to the *x*-axis, the flat-band potential V_{fb} is obtained and correcting for the standard potential of the Ag/AgCl electrode (that means addition of +0.2 V), V_{fb} of TiO_2, In_2O_3, Cu_2O, TiO_2/In_2O_{3calc},TiO_2/In_2O_{3sonic} and ternary hybrid was calculated to be −0.04 V, −0.27, −0.31, −0.59, −0.47 and −0.18 *vs.* NHE (normal hydrogen electrode), respectively. The flat-band potential can be approximate as *quasi Fermi level* and lies 0.1 V lower the conduction band minimum (CBM) [44]. Thus, the E_{CB} was estimated to be −0.14 V for TiO_2, -0.37 V for In_2O_3, -0.41 V for Cu_2O, −0.69 V for TiO_2/In_2O_{3calc}, −0.57 V for $TiO_2/In_2O_{3\ sonic}$ and −0.28 V for the ternary hybrid respectively.

It is evident a progressive negative shift of V_{fb} and hence in E_{CB} passing from pure TiO_2 to TiO_2/In_2O_3 obtained by sonication and by calcination. Knowing the relation between the carrier density N_D and the slope k of the linear portion of the Mott-Schottky graph [45] according to equation 1 below, where e, ε, ε' are the elementary electron charge, dielectric constant and permittivity in vacuum respectively, it was calculated the value for N_D in pure TiO_2 which resulted 7.58×10^{19} that increases progressively to 1.21×10^{20} for $TiO_2/In_2O_{3\ sonic}$ and becomes almost double for $TiO_2/In_2O_{3\ calc}$ being N_D=2.05×10^{20}.

$$N_D = \frac{2}{\varepsilon \cdot \varepsilon' \cdot e \cdot k} \quad (equation\ 1)$$

Correspondingly, the charge transfer rate from the bulk to the surface is dramatically increased and this justifies the enhanced reaction rate of

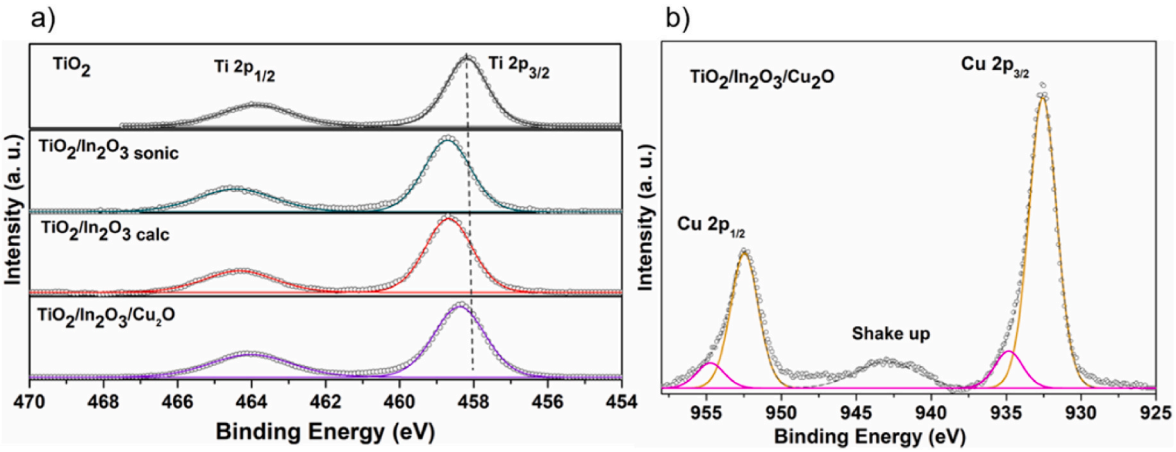

Fig. 5. (a) Comparison of Ti 2p core-level XPS spectra of various samples; (b) Cu 2p core-level XPS spectrum of $TiO_2/In_2O_3/Cu_2O$.

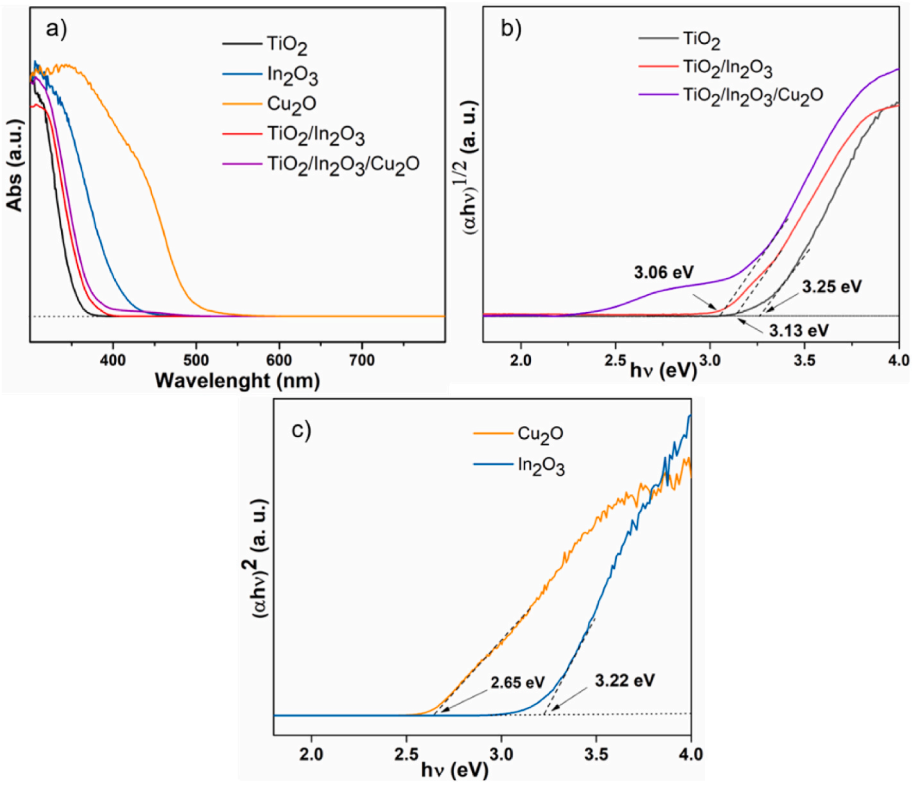

Fig. 6. a) UV–Vis diffuse reflectance spectra of all the samples, b) Tauc plots of TiO_2, TiO_2/In_2O_3, $TiO_2/In_2O_3/Cu_2O$, c) Tauc plots of In_2O_3 and Cu_2O.

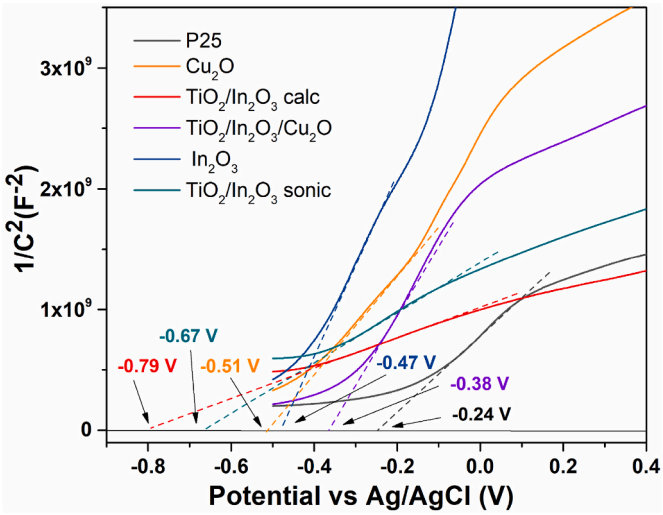

Fig. 7. Mott-Schottky plots of pristine TiO_2, TiO_2/In_2O_3 $_{sonic}$, TiO_2/In_2O_3 $_{calc}$ and $TiO_2/In_2O_3/Cu_2O$. Dashed lines show an approximate linear fit used to estimate the $V_{fb.}$

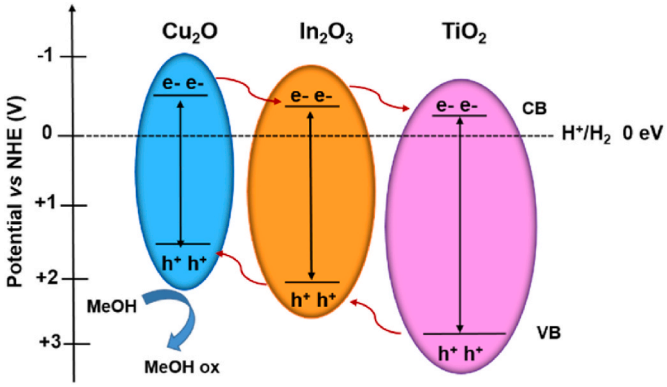

Fig. 8. Band energy level diagram and the proposed pathway for the photo-generated charge carriers over $TiO_2/In_2O_3/Cu_2O$ under UV–Vis irradiation.

4.4 times passing from TiO_2 to TiO_2/In_2O_3 $_{sonic}$ and of 18 times going to TiO_2/In_2O_{3calc}.

From the Mott-Schottky data, the energy position of the valence band could also be calculated according to: $E_{VB} = E_{CB} + E_g$ where E_g is the band gap of the semiconductors shown above in Fig. 6b–c. From these experimental magnitudes, the band energy level diagram could be derived as shown in Fig. 8.

The photoluminescence spectra of TiO_2, In_2O_3, TiO_2/In_2O_{3calc} and $TiO_2/In_2O_3/Cu_2O$ samples were measured to examine the transfer, migration and recombination process of the photo-induced charge carriers under the excitation wavelength of 325 nm. The sharpness of PL intensity peaks depends on the recombination of electron/hole pairs. As shown in Fig. 9, In_2O_3 reveals the strongest luminescence peak at about 458 nm. Meanwhile, the PL emission band for TiO_2/In_2O_3 was weaker which demonstrates that indium accelerate e−/h + pairs separation. A further reduction in PL intensity was observed after loading Cu_2O NPs to get the final ternary heterostructure, where the synergistic effect of copper and indium favored a better separation of photo-induced charge carriers on titania surface and a faster migration of charges to the surface, hence an improved photocatalytic activity is expected for the ternary respect to the binary nanocomposite.

To evaluate the interface charge mobility in the binary and ternary composites applied in HER, EIS measures were carried out. Intriguingly, TiO_2/In_2O_3 prepared by calcination showed a smaller arc radius than the corresponding binary obtained by sonication see Fig. 9b, demonstrating a much more efficient charge transfer.

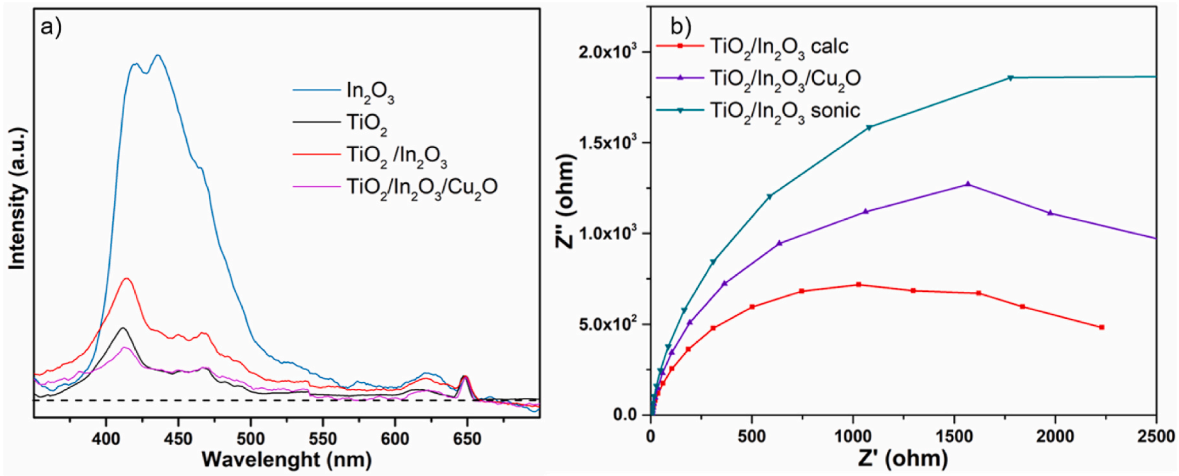

Fig. 9. a) Photoluminescence spectra of TiO_2, In_2O_3, TiO_2/In_2O_3 and $TiO_2/In_2O_3/Cu_2O$; b) Nyquist plot measured under a bias of potential of 0.3 V (vs. Ag/AgCl) in 0.5 M Na_2SO_4 solution. The symbols correspond to the measured data and the lines represent the fitting results.

3.2. *Photocatalytic activity for hydrogen evolution*

The synthesized composites were tested on the process of water splitting carried out by means of photoactivation. A 300 Watt Xenon lamp was used as source of light and the catalyst was dispersed in water with a concentration of 0.43 mg/mL. The effect of different synthetic strategy, either calcination or sonication, the calcination temperature and co-catalyst (indium, copper) loading on TiO_2 were analysed. The binary composite TiO_2/In_2O_3 was prepared with 3.5, 5.0 and 10.0 wt% of In_2O_3 content respectively, by ultrasonicating the dispersion of the two oxides in isopropanol. Surprisingly only the binary with 3.5 wt% In_2O_3 was active and gave a hydrogen productivity of 0.8 mmol/g·h. Aiming to obtain a tighter interaction between TiO_2 and In_2O_3, the synthesis of the binary was performed by following another strategy: different amount of preformed $In(OH)_3$ was assembled with TiO_2 by 1 h of sonication and afterwards the isolated white powder was calcined at T = 600 °C. The corresponding binary TiO_2/In_2O_3 having 0.5, 1.5, 3.5 and 5.0 wt% respectively of In_2O_3 grown *in situ*, were tested and the best catalytic activity was observed again for 3.5 wt% In_2O_3, which gave a hydrogen production of 3.5 mmol/g·h, that is 4.4 times higher than the analogous TiO_2/In_2O_3 prepared by sonication, see Fig. 10a, where it is added for comparison pure TiO_2 that gave very low H_2 production (0.2 mmol/g h). Meanwhile the other binary nanocomposites TiO_2/In_2O_3 obtained by calcination at T = 600 °C were inactive. To verify whether the calcination temperature plays any effect, the best performing photocatalyst TiO_2/In_2O_3 (3.5 wt%), was prepared by heating up the precursors $TiO_2/In(OH)_3$ at 400, 500 and 700 °C respectively for 2 h in argon atmosphere. The results of the catalytic tests are shown in Fig. 10b

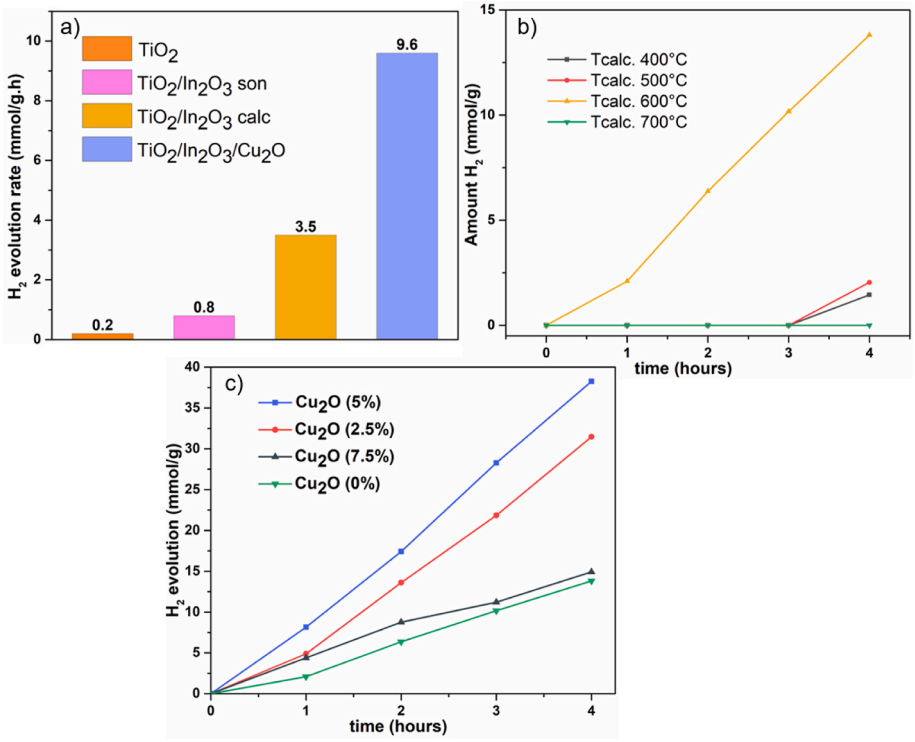

Fig. 10. a) Comparison of pure TiO_2, binary and ternary photocatalysts in the rate of HER. b) Effect of calcination temperature of TiO_2/In_2O_3 on the amount of hydrogen evolution. c) Influence of Cu_2O (wt%) on the amount of hydrogen evolution of the corresponding photocatalyst $TiO_2/In_2O_3/Cu_2O$.

and surprisingly it was observed the calcination at T = 600 °C was by far the best one in creating an efficient heterojunction between In_2O_3 and TiO_2. Heating at 700 °C there was no activity, and going to a temperature lower than 600 °C, it was observed a long induction period of 3 h and afterwards a modest catalytic activity was measured, see Fig. 10a.

A dramatic increase in catalytic activity was observed when to the binary TiO_2/In_2O_3 calc different amount (2.5, 5.0, 7.5%) of preformed Cu_2O NPs were loaded via ultrasonication. As shown in Fig. 10c, the maximum photocatalytic activity was reached with a 5 wt% Cu_2O that gave 9.6 mmol/g·h of H_2, almost 50 times the production observed with pure TiO_2, and overwhelms similar TiO_2-based photocatalysts which have been collected in Table S2 for comparison. A further increase of Cu_2O NPs to 7.5 wt % had the opposite effect of decreasing the activity likely due to shielding of light.

A screening of hole scavengers was carried out firstly on the binary TiO_2/In_2O_3, substituting methanol with either ethanol or glycerol and keeping their amount fixed to 20 vol%, but no catalytic activity was observed. On the other hand, diminishing the amount of methanol from 20 to 10 vol%, the H_2 production was lowered to 1.4 mmol/g·h.

A photo-stability test of the ternary catalyst was performed over four consecutive runs, with each run of 3 h, as shown in Fig. S9. After each run, the light irradiation was stopped, the reactor was open to evacuate the hydrogen gas and then refilled with nitrogen at 1.0 bar. After the first and the second run, the hydrogen production decreases, passing from 9.4 to 7.8 and 6.6 mmol/h·g, meanwhile was left unaltered after the third and fourth run. The diminution of the catalytic activity can be inferred to an incipient degradation of Cu_2O that is well known to be subjected to photocorrosion and to loose the catalytic efficiency [46,47]. The XRD analysis of the catalyst recovered after the fourth run confirmed the incipient oxidation of Cu_2O with a tiny amount of CuO as shown in Fig. S10. The morphology of the recovered catalyst was unaltered and there was no aggregation of the nanostructures as evidenced by SEM image in Fig. S11.

4. Conclusion

Successful fabrication of the binary TiO_2/In_2O_3 heterostructure was achieved by a straightforward and easy protocol. Two different strategies were followed: a) ultrasonication of preformed In_2O_3 with TiO_2 NPs or b) calcination of the precursor $In(OH)_3$ mixed with TiO_2 NPs. The latter route afforded an increase in the photocatalytic activity by a factor of 18 respect to the benchmark TiO_2, revealing the *in situ* growth brings about the construction of a much stronger interfacial interaction between TiO_2 and In_2O_3 as revealed by the shift of Raman signals of In_2O_3 and XPS signals of TiO_2. The formation of a TiO_2/In_2O_3 heterojunction constitutes a preferential channel that greatly promotes the interfacial charge transfer, as assessed by EIS measures and a largely increased carrier density N_D is present in the material as shown by Mott-Shottky plot. By loading on the n-type TiO_2/In_2O_3 composite a p-type semiconductor as Cu_2O NPs, an electric field is created at the interface that impedes the charge recombination as shown by PL measures. In conjunction with this, the deeper light absorption in the visible region of Cu_2O contributes to a further three folds enhancement of hydrogen productivity, reaching 9.6 mmol/h·g, which is *48 times* higher than pristine TiO_2 without using any noble metal as co-catalyst. This contribution provides a preliminary study that paves the way to the exploitation of other inorganic substrates for solar fuels production by finely tuning their catalytic activity through suitable synthetic conditions.

Declaration of competing interest

The authors declare that they have no known competing financial interests or personal relationships that could have appeared to influence the work reported in this paper.

Acknowledgements

M.C. thanks the project "FERMAT - Fast ElectRon dynamics in novel hybrid organic-2D MATerials" funded by the MUR Progetti di Ricerca di Rilevante Interesse Nazionale (PRIN) Bando 2017 - Grant number 2017KFY7XF for financing a post-doctoral grant to S. I. at ICCOM CNR. This research project has been partially funded by the European Union - NextGenerationEU under the Italian Ministry of University and Research (MUR) National Innovation Ecosystem grant ECS00000041 - VITALITY. M. C acknowledges Università degli Studi di Perugia and MUR for support within the project Vitality. The authors are very grateful to Mr. Carlo Bartoli (CNR ICCOM) for the technical assistance and for constructing the Teflon-lined autoclave used for the hydrothermal synthesis.

Appendix A. Supplementary data

Supplementary data to this article can be found online at https://doi.org/10.1016/j.ijhydene.2024.03.162.

References

[1] Riera JA, Lima RM, Knio OM. A review of hydrogen production and supply chain modeling and optimization. Int J Hydrogen Energy 2023;48:13731–55. https://doi.org/10.1016/j.ijhydene.2022.12.242.
[2] Abe JO, Popoola API, Ajenifuja E, Popoola MO. Hydrogen energy, economy and storage: review and recommendation. Int J Hydrogen Energy 2019;44:15072–86. https://doi.org/10.1016/j.ijhydene.2019.04.068.
[3] Song H, Luo S, Huang H, Deng B, Ye J. Solar-driven hydrogen production: recent advances, challenges, and future perspectives. ACS En. Lett. 2022;7:1043–65. https://doi.org/10.1021/acsenergylett.1c02591.
[4] Tao X, Zhao Y, Wang S, Li C, Li R. Recent advances and perspectives for solar-driven water splitting using particulate photocatalysts. Chem Soc Rev 2022;51:3561–608.
[5] Zhan X, Fang Z, Li B, Zhang H, Xu L, Hou H, Yang W. Rationally designed Ta_3N_5@ReS_2 heterojunctions for promoted photocatalytic hydrogen production. J Mater Chem A 2021;9:27084–94.
[6] Lan Q, Jin S, Yang B, Zhao Q, Si C, Xie H, Zhang Z. Metal-oxo cluster catalysts for photocatalytic water splitting and carbon dioxide reduction. Trans Tianjin Univ 2022;28:214–25. https://doi.org/10.1007/s12209-022-00324-z.
[7] Zhan X, Zheng Y, Li B, Fang Z, Yang H, Zhang H, Xu L, Shao G, Hou H, Yang W. Rationally designed $Ta_3N_5/ZnIn_2S_4$ 1D/2D heterojunctions for boosting Visible-Light-driven hydrogen evolution. Chem Eng J 2022;431:134053. https://doi.org/10.1016/j.cej.2021.134053.
[8] Chen X, Mao S. Titanium dioxide nanomaterials: synthesis, properties, modifications and applications. Chem Rev 2007;107:2891–959. https://doi.org/10.1021/cr0500535.
[9] Hendon CH, Tiana D, Fontecave M, Sanchez C, D'Arras L, Sassoye C, Rozes L, Mellot-Draznieks C, Walsh A. Engineering the optical response of the titanium-MIL-125-metal-organic framework through ligand functionalization. J Am Chem Soc 2013;135:10942–5. https://doi.org/10.1021/ja405350u.
[10] Tan Y, Liu M, Wei D, Tang H, Feng X, Shen S. A simple green approach to synthesis of sub-100 nm carbon spheres as template for TiO_2 hollow nanospheres with enhanced photocatalytic activities. Sci China Mater 2018;61:869–77. https://doi.org/10.1007/s40843-017-9183-2.
[11] Fang S, Liu Y, Sun Z, Lang J, Bao C, Hu YH. Photocatalytic hydrogen production over Rh-loaded TiO_2: what is the origin of hydrogen and how to achieve hydrogen production from water? Appl Catal B 2020;278:119316. https://doi.org/10.1016/j.apcatb.2020.119316.
[12] Jin ZL, Jiang XD, Guo X. Hollow tubular Co_9S_8 grown on In_2O_3 to form S-scheme heterojunction for efficient and stable hydrogen evolution. Int J Hydrogen Energy 2022;47:1669–82. https://doi.org/10.1016/j.ijhydene.2021.10.151.
[13] Liu ML, Li P, Wang SJ, Liu YM, Zhang JQ, Chen L, Wang JM, Liu YS, Shen Q, Qu P, Sun HQ. Hierarchically porous hydrangea-like In_2S_3/In_2O_3 heterostructures for enhanced photocatalytic hydrogen evolution. J Colloid Interface Sci 2021;587:876–82. https://doi.org/10.1016/j.jcis.2020.11.048.
[14] Wen L, Renqiang Y, Ligong Z, Qingbing M, Zhenghua W, Jinfeng Z, Zhen L. Highly efficient photocatalytic decomposition of triazophos using novel In_2O_3/WO_3 nanocomposites with oxygen defects and S-Scheme heterojunctions. Int J Hydrogen Energy 2024;57:369–78. https://doi.org/10.1016/j.ijhydene.2024.01.061.
[15] Yang YX, Pan YX, Tu X, Liu CJ. Nitrogen doping of indium oxide for enhanced photocatalytic reduction of CO_2 to methanol. Nano Energy 2022;101:107613. https://doi.org/10.1016/j.nanoen.2022.107613.
[16] Mohamed RM, Ismail AA, Basaleh AS, Bawazir HA. Facile fabrication of mesoporous $In_2O_3/LaNaTaO_3$ nanocomposites for photocatalytic H_2 evolution. Int J Hydrogen Energy 2020;45:19214–25. https://doi.org/10.1016/j.ijhidene.2020.05068.

[17] Hu LJ, Yang HL, Wang SH, Gao JL, Hou HL, Yang WY. MOF-derived hexagonal In_2O_3 microrods decorated with g-C_3N_4 ultrathin nanosheets for efficient photocatalytic hydrogen production. J Mater Chem C 2021;9:534–5348. https://doi.org/10.1039/D1TC00973G.
[18] Wang MG, Wang X, Wang M, Han J. Mesoporous In_2O_3 nanorods/In_2S_3 nanosheets hierarchical heterojunctions toward highly efficient visible light photocatalysis. J Alloys Compd 2022;921:165973.
[19] Tian Y, Hong Y, Chen B, Zhang K, Hong D, Lin X, Shi J. Facile template-free fabrication of different micro/nanostructured In_2O_3 for photocatalytic H_2 production from glucose solution. Int J Hydrogen Energy 2024;51:475–87. https://doi.org/10.1016/j.ijhydene.2023.08.223.
[20] Mu J, Chen B, Zhang M, Guo Z, Zhang P, Zhang Z, Sun Y, Shao C, Liu Y. Enhancement of the visible-light photocatalytic of In_2O_3-TiO_2 nanofiber heteroarchitectures. ACS Appl Mater Interfaces 2012;4:424–30.
[21] Tahir M, Amin NS. Indium-doped TiO_2 nanoparticles for photocatalytic CO_2 reduction with H_2O vapors to CH_4. Appl Catal B Environ 2015;162:98–109. https://doi.org/10.1016/j.apcatb.2014.06.037.
[22] Du Q, Ma J, Shao X, Wang W, Tian G. Core-shell structured TiO_2@In_2O_3 for highly active visible-light photocatalysis. Chem Phys Lett 2019;714:208–12. https://doi.org/10.1016/j.cplett.2018.11.004.
[23] Umer M, Tahir M, Azam MU, Tahir B, Musaab M. Self-doped Ti^{3+} mediated TiO_2/In_2O_3/SWCNTs heterojunction composite under acidic/basic heat medium for boosting visible light induced H_2 evolution. Int J Hydrogen Energy 2019;44:13466–79. https://doi.org/10.1016/j.ijhydene.2019.04.020.
[24] Yang XW, Hou HL, Yang Y, Ma GZ, Zhan XQ, Yang HL, Yang WY. MXene-derived anatase-TiO_2/rutile-TiO_2/In_2O_3 heterojunctions toward efficient hydrogen evolution. Colloids Surf A Physicochem Eng Asp 2022;652:129881. https://doi.org/10.1016/j.colsurfa.2022.129881.
[25] Vinothkumar N, De M. Hydrogen production from water-methanol solution over visible light active indium-titanium oxide photocatalysts modified with copper oxide. Int J Hydrogen Energy 2014;39:11494–500.
[26] Rej S, Bisetto M, Naldoni A, Fornasiero P. Well-defined Cu_2O photocatalysts for solar fuels and chemicals. J Mater Chem A 2021;9:5915–51. https://doi.org/10.1039/d0ta10181h.
[27] Wang Y, Cao S, Huan Y, Nie T, Ji Z, Bai Z, Cheng X, Xi J, Yan X. The effect of composite catalyst on Cu_2O/TiO_2 heterojunction photocathodes for efficient water splitting. Appl Surf Sci 2020;526:146700. https://doi.org/10.1016/j.apsusc.2020.146700.
[28] Rezaee M, Khoie SMM, Liu KH. The role of brookite in mechanical activation of anatase-to-rutile transformation of nanocrystalline TiO_2: an XRD and Raman spectroscopy investigation. CrystEngComm 2011;13:5055–61. https://doi.org/10.1039/c1ce05185g.
[29] Howard CJ, Sabine TM, Dickson F. Structural and thermal parameters for rutile and anatase. Acta Crystallogr B 1991;47:462–8. https://doi.org/10.1107/s010876819100335x.
[30] Berengue OM, Rodrigues AD, Dalmaschio CJ, Lanfredi AJC, Leite ER, Chiquito AJ. Structural characterization of indium oxide nanostructures: a Raman analysis. J Phys D Appl Phys 2010;43:045401. https://doi.org/10.1088/0022-3727/43/4/045401.
[31] Zhu H, Wang N, Wang L, Yao K, Shen X. In situ X-ray diffraction study of the phase transition of nanocrystalline in$(OH)_3$ to In_2O_3. Inorg Mater 2005;41:609–12. https://doi.org/10.1007/s10789-005-0178-x.
[32] Mai NTT, Neto MM, Thang PV, Trung NN, Tu NC, Dung TN, Chinh HD, Anh LTL. Cu_2O nanoparticles: a simple synthesis, characterization and its photocatalytic performance toward methylene blue. Mater Trans 2020;61:1868–73. https://doi.org/10.2320/matertrans.MT-MN2019039.
[33] Raut NC, Mathews T, Chandramohan P, Srinivasan MP, Dash S, Tyagi AK. Effect of temperature on the growth of TiO_2 thin films synthesized by spray pyrolysis: structural, compositional and optical properties. Mater Res Bull 2011;46:2057–63.
[34] Shanmuganathan V, Kumar JS, Pachaiappanb R, Thangadurai P. Transition metal ion-doped In_2O_3 nanocubes: investigation of their photocatalytic degradation activity under sunlight. Nanoscale Adv 2021;3:471–85. https://doi.org/10.1039/D0NA00694G.
[35] Arooj S, Xu TT, Hou X, Wang Y, Tong J, Chu J, Liu B. Green emission of indium oxide via hydrogen treatment. RSC Adv 2018;8:11828–33. https://doi.org/10.1039/C8RA00654G.
[36] Khan A, Rahman F, Nonjai R, Asokan K. Structural, optical and electrical transport properties of Sn doped In_2O_3. Solid State Sci 2020;109:106436. https://doi.org/10.1016/j.solidstatesciences.2020.106436.
[37] Boonprakob N, Wetchakun N, Phanichphant S, Waxler D, Sherrell P, Nattestad A, Chen J, Inceesungvorn B. Enhanced visible-light photocatalytic activity of g-C_3N_4/TiO_2 films. J Colloid Interface Sci 2014;417:402–9. https://doi.org/10.1016/j.jcis.2013.11.072.
[38] Aguirrea ME, Zhoub R, Eugene AJ, Guzmanb MI, Grela MA. Cu_2O/TiO_2 heterostructures for CO_2 reduction through a direct Z-scheme: protecting Cu_2O from photocorrosion. Appl Catal B Environ 2017;217:485–93. https://doi.org/10.1016/j.apcatb.2017.05.058.
[39] Ma D, Shi J-W, Zou Y, Fan Z, Shi J, Cheng L, Sun D, Wang Z, Niu C. Multiple carrier-transfer pathways in a flower-like In_2S_3/$CdIn_2S_4$/In_2O_3 ternary heterostructure for enhanced photocatalytic hydrogen production. Nanoscale 2018;10:7860–70. https://doi.org/10.1039/C8NR00170G.
[40] Wang M, Sun L, Lin Z, Cai J, Xie K, Lin C. P-n Heterojunction photoelectrodes composed of Cu_2O-loaded TiO_2 nanotube arrays with enhanced photoelectrochemical and photoelectrocatalytic activities. Energy Environ Sci 2013;6:1211–20. https://doi.org/10.1039/C3EE24162A.
[41] Zou X, Yuan C, Cui Y, Dong Y, Chen D, Ge H, Ke J. Construction of zinc-indium-sulfide/indium oxide step-scheme junction catalyst for enhanced photocatalytic activities of pollutant degradation and hydrogen generation. Separ Purif Technol 2021;266:118545. https://doi.org/10.1016/j.seppur.2021.118545.
[42] Liu J, Ke J, Li D, Sun H, Liang P, Duan X, Tian W, Tadé MO, Liu S, Wang S. Oxigen vacancies in shape controlled Cu_2O/reduced graphene oxide/in$_2O_3$ hybrid for promoted photocatalytic water oxidation and degradation of environmental pollutants. ACS Appl Mater Interfaces 2017;9:11678–88. https://doi.org/10.1021/acsami.7b01605.
[43] Ke J, Zhou HR, Liu J, Zhang ZG, Duan XG, Wang SB. Enhanced light-driven water splitting by fast electron transfer in 2D/2D reduced graphene oxide/tungsten trioxide heterojunction with preferential facets. J Colloid Interface Sci 2019;555:413–22. https://doi.org/10.1016/j.jcis.2019.08.008.
[44] Gao W, Bai X, Gao Y, Liu J, He H, Yang Y, Han Q, Wang X, Wu X, Wang J, Fan F, Zhou Y, Li C, Zou Z. Anchoring of black phosphorus quantum dots onto WO_3 nanowires to boost photocatalytic CO_2 conversion into solar fuels. Chem Commun 2020;56:7777–80. https://doi.org/10.1039/D0CC00805B.
[45] Tahir B, Tahir M. Morphological effect of 1D/1D In_2O_3/TiO_2 NRs/NWs heterojunction photo-embedded with Cu-NPs for enhanced photocatalytic H_2 evolution under visible light. Appl Surf Sci 2020;506:145034. https://doi.org/10.1016/j.apsusc.2019.145034.
[46] Toe CY, Zheng Z, Wu H, Scott J, Amal R, Yang YH. Photocorrosion of cuprous oxide in hydrogen production: rationalising self-oxidation or self-reduction. Angew Chem 2018;57:13613. https://doi.org/10.1002/anie.201807647.
[47] Toe CY, Scott J, Amal R, Ng YH. Recent advances in suppressing the photocorrosion of cuprous oxide for photocatalytic and photoelectrochemical energy conversion. J. of Phot. And Phot. C: Phot. Reviews 2019;40:191–211. https://doi.org/10.1016/j.jphotochemrev.2018.10.001.